

Synthetic Aperture Focusing for Short-Lag Spatial Coherence Imaging

Nick Bottenus, Brett C. Byram, *Member, IEEE*, Jeremy J. Dahl, *Member, IEEE*,
and Gregg E. Trahey, *Member, IEEE*

Abstract—It has been demonstrated that short-lag spatial coherence (SLSC) ultrasound imaging can provide improved speckle SNR and lesion CNR compared with conventional B-mode images, especially in the presence of noise and clutter. Application of the van Cittert–Zernike theorem predicts that coherence among the ultrasound echoes received across an array is reduced significantly away from the transmit focal depth, leading to a limited axial depth of field in SLSC images. Transmit focus throughout the field of view can be achieved using synthetic aperture methods to combine multiple transmit events into a single final image. A synthetic aperture can be formed with either focused or diverging transmit beams. We explore the application of these methods to form synthetically focused channel data to create SLSC images with an extended axial depth of field. An analytical expression of SLSC image brightness through depth is derived for the dynamic receive focus case. Experimental results in a phantom and *in vivo* are presented and compared with dynamic receive focused SLSC images, demonstrating improved SNR and CNR away from the transmit focus and an axial depth of field four to five times longer.

I. INTRODUCTION

THE van Cittert–Zernike (VCZ) theorem describes the spatial coherence of a wave field produced by an incoherent source. More specifically for ultrasound, the VCZ theorem predicts the similarity between echo signals received on spatially separated transducer elements. For a spatially incoherent medium, the coherence is related to the Fourier transform of the product of the intensity distribution of the transmitted beam and the square of the reflectivity function of the insonified medium. Mallart and Fink [1] and Liu and Waag [2] analyzed spatial coherence for ultrasound, demonstrating that the coherence function for a region of diffuse (randomly positioned, sub-wavelength sized) scatterers decreases linearly out to the length of the transducer, assuming a rectangular apodization, whereas a compact target has a constant coherence function at unity. Signals away from the transmit focal depth show decreased spatial coherence, as in Fig. 1.

Several groups have extended this idea to analyze signals based on their coherence, augmenting existing imaging methods by excluding signals with aberration or off-axis scattering [3], [4]. Recently, our group introduced an imaging technique called short-lag spatial coherence (SLSC) imaging that utilizes only coherence information to form an image rather than using coherence to enhance the echo brightness signal [5]. Each pixel in an SLSC image is formed by integrating the measured coherence at small element separations, or lags. SLSC imaging takes advantage of the differentiation of structures by coherence in the short-lag region, where the difference between the curves is most evident. It has been shown that in many cases SLSC images demonstrate improved speckle SNR and contrast-to-noise ratio (CNR) compared with B-mode images [5]–[7].

Although there are benefits to using SLSC imaging over conventional B-mode imaging, the VCZ theorem predicts a reduction in coherence away from the transmit focal depth. Dynamic receive focusing improves the lateral point spread function through depth in B-mode imaging, making the resulting image fairly uniform in texture size despite a fixed transmit focus. Although applying receive delays is necessary in SLSC imaging to align signals before correlating the returned echoes, there is not an equivalent receive focusing process that changes the shape of the coherence curve. SLSC images therefore demonstrate severely reduced uniformity in resolution and brightness away from the focal depth, especially in the near-field of the image. This reduced axial depth of field limits diagnostic value, particularly in fine anatomical structures requiring high CNR and SNR to resolve. One solution used previously was to acquire multiple data sets with different transmit focal points, stitching together the acquisitions in post-processing to increase the axial depth of field. This method improves image quality but requires reduction of the frame rate to perform multiple acquisitions at successive transmit focal depths. This also leaves poor quality regions in the image caused by spaces between the chosen foci.

To address this problem, we propose using synthetic aperture focusing to achieve transmit focus throughout the field and improve coherence, and therefore image uniformity, at all depths. We briefly introduce three synthetic aperture focusing techniques and their relations to SLSC image formation. We demonstrate experimental images and image metrics from an anechoic lesion phantom and *in vivo* images from the human thyroid to show clinical applicability.

Manuscript received December 20, 2012; accepted May 27, 2013. This work was supported by National Institutes of Health (NIH) grants R01-EB013361 and T32-EB001040 from the National Institute of Biomedical Imaging and Bioengineering.

The authors are with the Biomedical Engineering Department, Duke University, Durham, NC (e-mail: nick.bottenus@duke.edu).

DOI <http://dx.doi.org/10.1109/TUFFC.2013.2768>

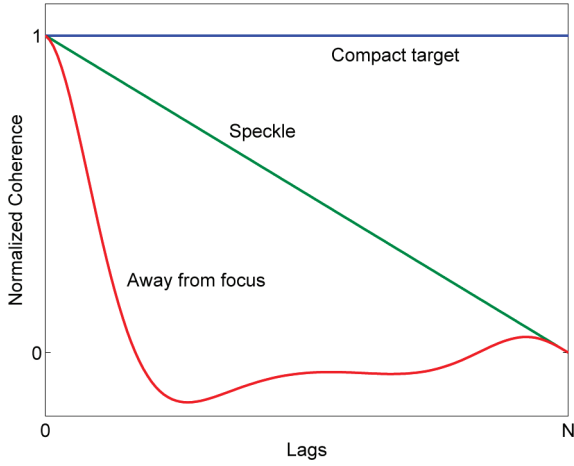


Fig. 1. Examples of estimated coherence functions of a laterally compact target and an extended fully developed speckle region at and away from the transmit focal depth. The coherence functions, calculated by correlation between received RF signals, are plotted as a function of element spacing on an N -element array. 

II. THEORY

The beamforming process is described here in two steps—focusing of the channel data and image formation.

A. Focusing

The received backscattered echoes from a converging transmit wave are focused by accounting for the time-of-flight of the wavefront. The transmit and receive distances are converted to times and summed using the assumed sound speed to appropriately delay each receive channel signal. Fig. 2(a) shows the distances used in dynamic receive beamforming, assuming a fixed time to reach the focal point and calculating receive times from each axial depth. A single transmit event is used to focus data for a single lateral location, an A-line in the final image.

For a focal point at depth z_f with element position x_i and an assumed sound speed c , the necessary transit time $t_d(i)$ for dynamic receive focusing of receive channel i for point $(0, z_p)$ is calculated using the array geometry with the origin at the center of the array.

$$t_d(i) = t_{\text{tx}} + t_{\text{rx}} = \frac{z_p + \sqrt{x_i^2 + z_p^2}}{c} \quad (1)$$

In contrast, synthetic aperture methods focus images by calculating both the transmit and receive times for every point in the field. Frazier and O’Brien [8] proposed a technique for a single-element transmit beam using a focused piston transducer. The focal point can be seen as a virtual source that has a known transmit delay, emitting a spherically diverging wave over a particular axial opening angle. Bae and Jeong [9] expanded this to linear arrays in a technique called “bi-directional pixel-based focusing” to take advantage of the increase in lateral spatial frequency bandwidth using a larger receive array. The distance be-

tween the virtual source and the point of interest is used to correct the transmit time, allowing calculation of the transmit time of the converging wave to the point of interest and the receive time to each element of the receive array. Fig. 2(b) shows the delays viewed in terms of the isochronous contour at a particular radius from the virtual source. Any point at this radius shares the same transmit delay, whereas the axial and lateral positions determine the receive delay. The final image is created by combining the focused RF data from each transmit event into a single high-resolution image.

Using synthetic aperture focusing for a single transmit event, the transit time $t_d(i)$ for receive channel i for a point located at (x_p, z_p) is found using the array geometry.

$$t_d(i) = \frac{z_f \pm \sqrt{x_p^2 + (z_f - z_p)^2} + \sqrt{(x_i - x_p)^2 + z_p^2}}{c} \quad (2)$$

The plus or minus term is positive for points after the transmit focus and negative for points before the transmit focus. This term creates a discontinuity at the focal point, although this is not a problem for our imaging case. When it is desirable to remove this artifact, the focal point may be placed outside the field of view, as shown by Kim *et al.* [10]. Each subimage is only reconstructed within the hourglass-shaped region defined by the extent of the transmit elements and position of the virtual source. As detailed by Kortbek *et al.* [11] for a similar beamforming strategy, every point in the image will receive a different number of contributions from the set of transmit events and requires normalization. This is achieved by assuming a constant signal amplitude within the transmit pro-

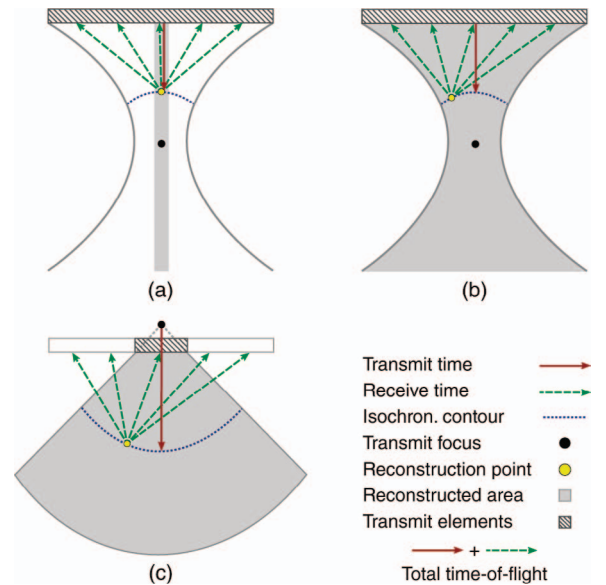


Fig. 2. Three focusing schemes. (a) Dynamic receive focusing creates a single A-line from each transmit event. (b) Focused transmit synthetic aperture forms a subimage from each transmit event within the hourglass-shaped area of the pulse. (c) Diverging transmit synthetic aperture forms a subimage from each transmit event within the fan-beam-shaped area of the pulse. 

file and dividing by the sum of the masks used to define the hourglass region for each transmit/receive event. The number of contributions to a given point depends on the distance between the virtual source and desired focal point and the focal gain of the transmit pulse.

The same idea can be used to place a source at or behind the physical array. Corl *et al.* [12] proposed acquiring a series of individual element firings to build up a complete data set that can be focused at any point in the field in post-processing. However, this case is not often practical due to electronic SNR limitations in firing a single element at a time. Karaman *et al.* [13] proposed firing a small subaperture of elements focused to simulate a virtual source point behind the array. Each subaperture transmits a diverging wave with curvature determined by the distance from the virtual source to each element. These virtual sources can then be used to calculate transmit time-of-flight and the physical receive elements can be used to calculate receive time-of-flight, shown in Fig. 2(c).

Using synthetic aperture focusing for a single transmit event with focus at $-z_f$, the transit time $t_d(i)$ for receive channel i for a point located at (x_p, z_p) is found using the array geometry.

$$t_d(i) = \frac{\sqrt{x_p^2 + (z_f + z_p)^2} + \sqrt{(x_i - x_p)^2 + z_p^2}}{c} \quad (3)$$

The total number of transmit events is reduced by the number of additional elements in the subaperture, reducing the effective transmit aperture size. The focused RF data from each subimage is summed to create a high-resolution image.

Although the subimage construct is useful for visualizing the focusing process, it is necessary for SLSC image formation to produce channel data rather than summed RF. The same time-of-flight equations can be used to focus the data, but each transmit and receive event must be abstracted to a virtual receive channel. This is straightforward for the diverging wave case because every transmit event uses the same set of receive elements, so the virtual array channels correspond directly to the receive channels and the lateral locations are the lateral lines chosen for focusing. For the focused transmit synthetic aperture, each transmit event corresponds to a different set of physical channels on the array. Each subimage only partially overlaps with the others, so the virtual channels from each transmit event only partially overlap as well. This leads to a virtual array larger than each individual transmit or receive aperture, but with only partial channel data.

B. Image Formation

The time-delayed RF channel data produced as discussed in the previous section are then used to create a final two-dimensional image. B-mode image formation is defined by the summation of the RF data across the channel dimension to create A-lines and envelope detection of the resulting lines to remove the carrier frequency. The

resulting envelope signals have a dynamic range of several orders of magnitude, so the images are displayed after logarithmic compression.

SLSC imaging uses the same set of time-delayed signals to calculate the spatial correlation between single-wavelength axial kernels from pairs of signals received at various receive element spacings [5]. The correlation values from all pairs at a given spacing are averaged to produce a single coherence value $\hat{R}(m)$ for that lag, creating a coherence curve at every axial and lateral point in the data set.

$$\hat{R}(m) = \frac{1}{N-m} \sum_{i=1}^{N-m} \frac{\sum_{n=n_1}^{n_2} s_i(n) s_{i+m}(n)}{\sqrt{\sum_{n=n_1}^{n_2} s_i^2(n) \sum_{n=n_1}^{n_2} s_{i+m}^2(n)}} \quad (4)$$

Each pixel R_{sl} in the final SLSC image is formed by integrating the resulting curve to a small number of lags M and normalizing by the maximum resulting value.

$$R_{sl} \propto \sum_{m=1}^M \hat{R}(m) \quad (5)$$

The result of this process is predicted by the combination of the VCZ theorem and the Fresnel diffraction integral for a region of diffuse scatterers. The Fresnel diffraction integral states that the pressure in the field, $P[x]$, from a linear-array transducer focused at depth z_f is given by a Fourier transform of the aperture $U[n]$ and the quadratic phase term resulting from propagation of the wave to a depth z [14]. The transducer has N elements with pitch w .

$$P[x] = \frac{e^{jkz}}{j\lambda z} e^{(jkx^2)/(2z)} \sum_{n=-\infty}^{\infty} (U[n] e^{(jknw^2)/(2z)}) e^{-2\pi j(x/(\lambda z))(nw)} \quad (6)$$

$$U[n] = e^{(-jknw^2)/(2z_f)} \text{rect}\left[\frac{n}{N}\right] \quad (7)$$

The aperture and additional phase term in parentheses can be combined into a single term, $U_1[n]$. Application of the VCZ theorem produces an expression for the SLSC pixel intensity for a given incoherent target $\chi[x]$. For a homogeneous speckle target, because the resulting SLSC value will be normalized by its maximum, $\chi[x] = 1$ can be used in this expression.

$$R_{sl} \propto \sum_{m=1}^M \text{FT}\{|P[x]\chi[x]|^2\} \propto \sum_{m=1}^M \text{FT}\{P[x]P^*[x]\} \quad (8)$$

The phase terms outside the Fourier transform of $U_1[n]$ cancel because of the complex conjugate term and the scaling term is removed by normalization. The Fourier transform of $U_1[n]$ is denoted by $\hat{U}_1[x]$.

$$R_{sl} \propto \sum_{m=1}^M \text{FT}\{\hat{U}_1[x]\hat{U}_1^*[x]\} \quad (9)$$

This expression can be reduced using the duality property and the Fourier transform relationship between multiplication and convolution.

$$R_{sl} \propto \sum_{m=1}^M (U_1[-n] * U_1^*[n])(m) \quad (10)$$

The result is simply the autocorrelation of the complex aperture, and provides the expected result of the VCZ theorem at the focus, where $z = z_f$ and the phase terms cancel. Walker and Trahey [15] arrived at a similar result for the effect of a thin screen aberrator on coherence, modeling the aberrator as a phase shift at the aperture. This provides a method to analyze coherence away from the transmit focus, allowing prediction of the depth of field of an SLSC image. The effective aperture varies because of the phase terms, making it sensitive to changes in element count, array pitch, frequency, and focal point.

Fig. 3 shows a sample set of coherence curves through depth for a 128-element, 7.5-MHz, $\lambda/2$ -pitch array with a transmit focus at 4 cm calculated using (10). In SLSC imaging, these curves are integrated over the short-lag region, up to $M = 20$ elements for the results shown in Fig. 4 for different choices of transmit focal point. The most defining characteristic of the curves is their asymmetry—the brightness falls off more slowly after the focus than it does before the focus because of the geometry of the wavefront. The curve gets broader as the focal point is moved deeper into the image with a fixed aperture, providing a larger depth of field.

It should be noted that SLSC pixel brightness is only a partial measure of image quality. Brightness is a normalized quantity, but it is not possible to achieve a more uniform SLSC image texture by applying normalization

through depth. This is because the brightness is related to the shape of the coherence curve, which itself is related to the pressure field. In B-mode imaging, the brightness is partially determined by attenuation and can be corrected using time-gain compensation without a change in focal properties. The closest analog in B-mode imaging to the SLSC brightness is the focal depth of field, defined as $7.2\lambda f_{\#}^2$ where $f_{\#}$ is the f-number or ratio of focal depth to aperture width, although the exact value can vary depending on the assumptions made [16]. For the case shown in Fig. 3, the expected B-mode depth of field would be 1.4 cm, compared with 3.6 cm using the -6 -dB points of the coherence curve. Although the SLSC depth of field is larger using these metrics, the image quality degrades more quickly outside of this region for SLSC than in B-mode because of the dependence on transmit focusing.

III. METHODS

A. Phantom and In Vivo Thyroid Experiments

RF channel data sets were collected using the Verasonics ultrasound scanner (Verasonics Inc., Redmond, WA) using an ATL L12-5 256-element linear array (multiplexed for 128 channels in transmit and receive) with pitch 0.195 mm using a center frequency of 7.5 MHz. All data sets were stored for offline processing.

The first phantom imaging target was a uniform 36-kPa CIRS elasticity phantom (Computerized Imaging Reference Systems Inc., Norfolk, VA) used to produce a speckle image. The imaging sequence acquired a linear B-mode scan using 128 contiguous imaging elements at 129 lateral imaging locations with a beamspace of a single element and transmit focus at 45 mm. A second scan was performed by firing on and recording from individual elements from the center 128 elements of the array, imaging the same location in the phantom. A third scan was per-

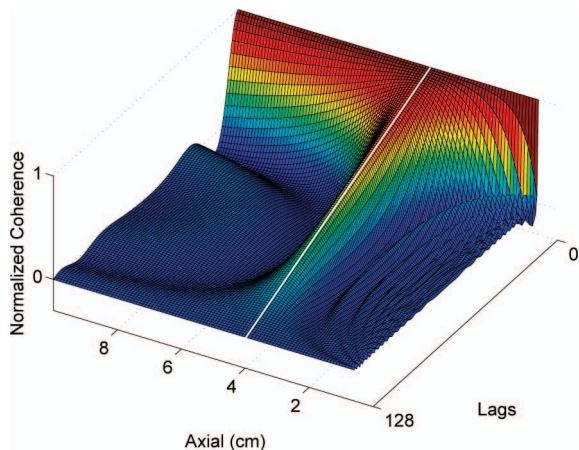


Fig. 3. Coherence curves through depth for a 4 cm transmit focus using (10). Note the linear curve at the 4 cm depth marked with a white line. Integration over the short-lag region predicts short-lag spatial coherence (SLSC) brightness. 

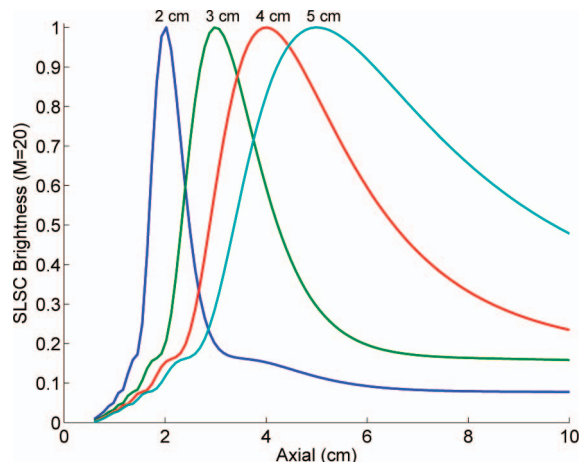


Fig. 4. Short-lag spatial coherence (SLSC) brightness (normalized) obtained by integrating coherence curves at various depths using (10). Curves shown for different focal points show that the shape of the curve depends on focal depth, among other parameters. 

formed by firing groups of 11 elements across the center 128 array elements with an f-number of 0.75, focused behind the array to produce a diverging wave.

The second phantom imaging target was a Gammex 408 LE Spherical Lesion Phantom (Gammex Inc., Middleton, WI) containing 4-mm-diameter anechoic lesions spaced 0.75 mm apart axially. Only the linear scan and 11-element synthetic aperture scan were performed for this target. The individual-element sequence was omitted from this procedure because of poor electronic SNR on the resulting signals, which will be discussed later in this paper.

In vivo channel data sets of the thyroid and surrounding structures were collected from a healthy 59-year-old male using the same imaging sequences as the lesion phantom. The acquisitions were performed with minimal time between sequences to produce similar views of the target. A flash Doppler sequence and native Verasonics color Doppler processing were used to provide real-time guidance for scanning vasculature.

B. RF Channel Data Processing

Each data set was focused using dynamic receive focusing to create a B-mode and SLSC image, as in Fig. 2(a). This same data set was used to perform focused transmit synthetic aperture focusing, as in Fig. 2(b), creating a matched B-mode and SLSC image over the same lateral and axial field of view. The central 128 virtual channels for each lateral location were used to produce the SLSC image. The diverging-wave data were processed to create a B-mode and SLSC image over the same field of view, as in Fig. 2(c).

In the uniform phantom, coherence curves were averaged over 4×4 mm square regions through depth.

In the anechoic lesion phantom, 3.5-mm-diameter circular regions inside and outside of the anechoic lesion at a depth of 22 mm were used to calculate contrast, CNR, and speckle SNR. The mean values inside and outside the lesion are μ_i and μ_o , and the variances inside and outside the lesion are σ_i^2 and σ_o^2 , respectively.

$$\text{Contrast} = 20 \log_{10}(\mu_i/\mu_o) \quad (11)$$

$$\text{CNR} = \frac{|\mu_i - \mu_o|}{\sqrt{\sigma_i^2 + \sigma_o^2}} \quad (12)$$

$$\text{SNR} = \mu_o/\sigma_o \quad (13)$$

-20 dB of Gaussian random noise was added to the raw data from the anechoic lesion phantom before beamforming to improve CNR [5]. Axial depth of field was plotted by averaging image brightness over a 1 mm lateral area between the lesions and using a moving average with a 6λ kernel axially.

For the *in vivo* data, power Doppler [16] and Kasai's algorithm for color flow imaging [17] were used to identify vasculature and produce a mask for the region of inter-

est. This mask and a 3×3 mm square region outside the masked region were used to calculate contrast, CNR, and SNR.

IV. RESULTS AND DISCUSSION

A. Uniform Phantom

Average coherence curves through depth are plotted for each focusing case in Fig. 5. The dynamic receive focusing case in Fig. 5(a) shows close to the expected linear shape only at the focal depth of 45 mm. This curve, barring aberration or other degrading effects, should linearly decrease from a coherence of 1 at zero lag and extend out to the full width of the array. All other curves show decreased coherence, especially in the short-lag region. At the shallowest depths, the curves approach a delta function, indicating little to no coherence between the receive channels. Decreased coherence in the short-lag region translates to poor image quality and reduced brightness in the SLSC image. This result supports the typical realization of SLSC images with a completely dark near-field and the coherence falling off slowly past the focal point, both of which are also predicted by the analytical expression.

The most striking observation of the focused transmit synthetic aperture in Fig. 5(b) is that the curve for each depth is approximately linear, indicating proper focusing, but each ends at a different number of lags. As described previously, each subaperture is properly focused at every depth but is made up of a different number of transmit elements based on the distance from the virtual source element and the opening angle of the source. The result at the focus is the same as in the dynamic receive case, with each of the 128 elements in the transmit aperture corresponding to physical elements. Before the transmit focus, fewer elements contribute to the wavefronts that trace out the isochronous volume and more virtual sources will likely not contribute. The effect beyond the transmit focus is similar but more subtle because of the distance from the array, so more elements contribute to any point on the wavefront. This is reflected in Fig. 5(b), where the curves past the focal point show roughly the same coherence. Because of these extra geometric effects, the virtual source approach to quantifying effective aperture size is misleading for this focusing scheme.

Curves at all depths for the single-element diverging wave synthetic aperture case in Fig. 5(c) are linear and extend to the full length of the array. However, the lag-1 coherence value of each curve decreases with depth because of the poor electronic SNR of the single-element transmit. Using (18), derived in Appendix A, the observed electronic SNR ranges from 9.9 dB to -6.5 dB at the measured depths. The noise-induced decrease in coherence makes this scheme a poor choice for SLSC imaging, so it is not considered in the other imaging tasks presented here.

An improvement to the single-element case can be made by transmitting a diverging wave on a small subap-

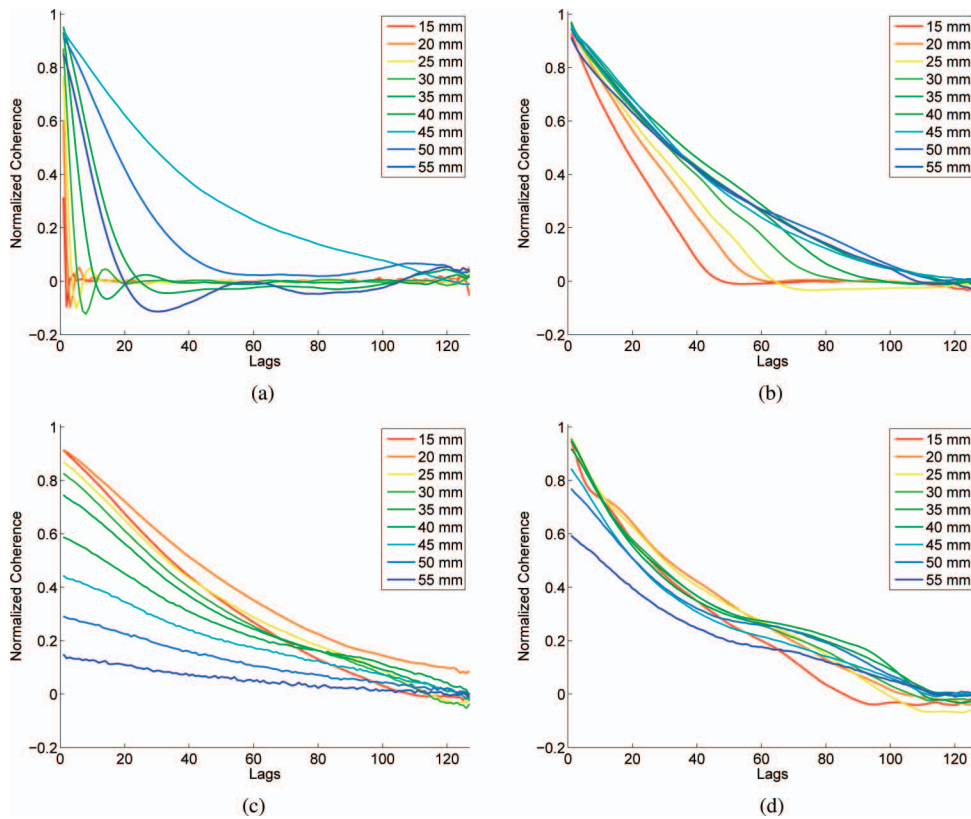


Fig. 5. Coherence curves through depth from a uniform phantom demonstrating differences in expected shape. (a) Dynamic receive has linear coherence only at the transmit focus at a depth of 45 mm. (b) Focused transmit synthetic aperture (45 mm transmit focus) has linear coherence at all depths but extends to different lags. (c) Single-element diverging wave synthetic aperture has linear coherence at all depths but has reduced coherence at depth due to electronic SNR. (d) 11-element diverging wave synthetic aperture has nearly linear coherence at all but the greatest depths due to improved electronic SNR. 

erture of 11 elements. All curves in Fig. 5(d) show similar coherence and have high coherence in the short-lag region. Although the curves represent properly focused images, an interesting effect can be seen in all cases in that they are not linear. The curves have a distinctive shape that is characteristic of apodization. This shape has a minimal effect on the short-lag region, but is more thoroughly explored in Appendix B.

B. Anechoic Lesion Phantom

The SLSC images for each acquisition and focusing scheme are shown in Fig. 6. A circular region of interest and a corresponding background region are outlined in the first plot and image quality metrics for these regions are listed in Table I. The average brightness over a 1 mm lateral region of uniform background is plotted in Fig. 7 to compare the depth of field of each image.

The dynamic receive image in Fig. 6(a) shows a limited depth of field, outside of which the image is dark and has overall poor image quality. As the transmit focus moves lower, the depth of field gets wider and extends the visible portion of the image. This pattern confirms the predictions made by the analytical expression for SLSC image brightness through depth.

Compared with the B-mode image, SLSC only makes a significant improvement in image metrics near the focal point. Contrast is slightly decreased, as expected from previous literature, but there is a large improvement in both CNR and SNR. When the transmit focus is anywhere but the lesion of interest, the lesion is difficult to resolve from the background and qualitatively worse than the B-mode image despite the misleading contrast measurement.

The focused transmit synthetic aperture image in Fig. 6(b) demonstrates a drastic improvement in depth of field, with good image quality throughout the entire field of view past the most shallow region, which is determined by the angular sensitivity of the array. All five transmit focal points produce similar images and maintain roughly the same image metrics for the region of interest. The improvements previously seen only at the focal point are now seen for all transmit focal depths.

The diverging transmit synthetic aperture produces a similar result to the focused transmit synthetic aperture scheme, as shown in Fig. 6(c). The electronic SNR at depth limits image quality more severely compared with the focused transmit. Both synthetic aperture techniques give substantial improvement over the previously published dynamic receive SLSC technique [5].

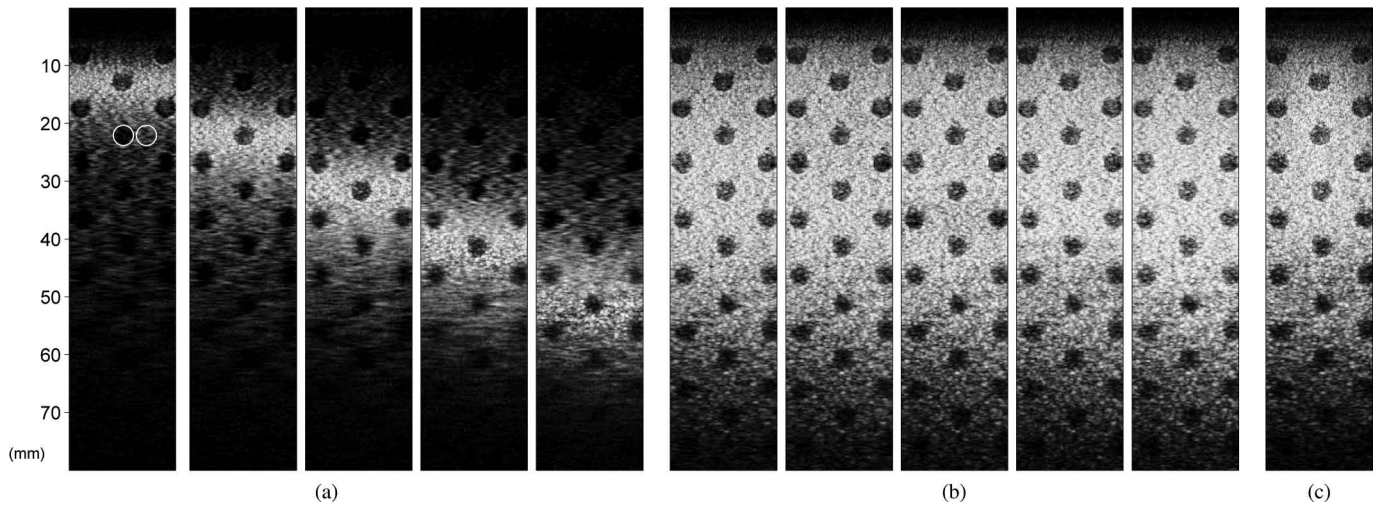


Fig. 6. Short-lag spatial coherence (SLSC) images ($M = 15$) of an anechoic lesion phantom with (a) dynamic receive, (b) focused transmit synthetic aperture, and (c) diverging transmit synthetic aperture focus. For (a) and (b), five images show transmit focus at 12.9, 22.0, 31.4, 41.1, and 51.1 mm. Regions of interest inside and outside lesion are shown circled in first image.

TABLE I. IMAGE QUALITY METRICS FOR ANECHOIC LESION PHANTOM.

Focus (mm)	B-mode			SLSC		
	Contrast (dB)	CNR	SNR	Contrast (dB)	CNR	SNR
Dynamic receive focus						
12.9	-10.6	1.2	1.8	-13.7	1.3	2.0
22.0	-12.0	1.3	1.8	-7.5	2.2	5.7
31.4	-10.8	1.3	1.9	-17.5	1.3	2.0
41.1	-10.6	1.2	1.9	-23.7	1.8	1.9
51.1	-10.2	1.2	1.9	-12.6	1.8	1.6
Focused synthetic aperture						
12.9	-12.4	1.3	1.8	-6.3	2.0	5.9
22.0	-12.1	1.1	1.5	-6.3	2.0	5.7
31.4	-11.8	1.3	1.8	-6.5	2.0	5.9
41.1	-11.7	1.3	1.8	-5.7	1.8	6.1
51.1	-11.4	1.3	1.8	-5.1	1.8	7.0
Diverging synthetic aperture						
N/A	-10.9		1.8	-5.2	1.6	6.1

SLSC = short-lag spatial coherence; CNR = contrast-to-noise ratio.

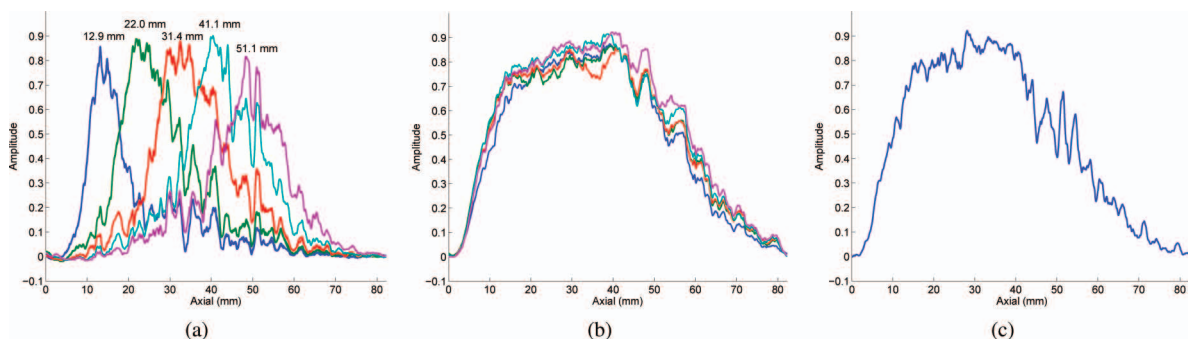


Fig. 7. Short-lag spatial coherence (SLSC) brightness ($M = 15$) for an anechoic lesion phantom averaged over a 1 mm lateral region through depth for (a) dynamic receive, (b) focused transmit synthetic aperture, and (c) diverging wave synthetic aperture focusing. The curves for each depth in (b) are indistinguishable and are not individually labeled.

TABLE II. IMAGE QUALITY METRICS FOR SMALL VASCULATURE IN HUMAN THYROID.

Type	Contrast (dB)	CNR	SNR
B-mode image			
Dynamic receive focus	-3.1	0.4	1.8
Focused synthetic aperture	-4.2	0.5	1.7
Diverging synthetic aperture	-3.8	0.4	1.7
SLSC image			
Dynamic receive focus	-12.6	0.7	1.2
Focused synthetic aperture	-8.1	1.2	3.1
Diverging synthetic aperture	-4.2	0.7	3.1

CNR = contrast-to-noise ratio; SLSC = short-lag spatial coherence.

C. In Vivo Thyroid

Fig. 8 shows the results of the three focusing schemes for both B-mode and SLSC imaging. The color flow Doppler image, thresholded using the power Doppler signal, shows small vasculature in the middle of the thyroid in Fig. 8(a). This hypoechoic target is used as the region of interest for image metric calculations with a 3-mm-square section of the background tissue at the same depth. The image quality metrics for this detection task are shown in Table II.

The dynamic receive SLSC image in Fig. 8(b) demonstrates poor image quality away from the focal point of 25 mm, showing only the lowest section of vasculature clearly. Before the focus, it is difficult to distinguish the vessel despite the expectation of uniform thyroid tissue around it. The focused transmit synthetic aperture restores the structure in this region, allowing full visualization of the vessel in Fig. 8(c) despite the large axial extent. The diverging wave synthetic aperture shows a similar result in Fig. 8(d) with a slightly different background texture resulting from poor electronic SNR compared with the focused transmit. Both methods show significant improvement over the dynamic receive SLSC method and clearly show the region of interest.

V. CONCLUSION

We have analytically described the restricted depth of field in dynamic receive SLSC imaging, a significant limitation compared with B-mode imaging. We have also shown that this issue can be resolved using synthetic aperture techniques, comparing three common methods and detailing their coherence properties. The focused transmit synthetic aperture technique makes it possible to produce matched images between dynamic receive and synthetic aperture, making it an appealing research technique.

The practical drawbacks to either technique, as have been reported in other synthetic aperture literature, are the computational cost of post-processing the data and motion artifacts [18]. As work continues to be done to implement such algorithms on largely parallel GPU or CPU systems, we expect these methods to become feasible for real-time scanning.

APPENDIX A

DECORRELATION CAUSED BY ADDITIVE NOISE ON AN ARRAY

The correlation coefficient is a convenient metric measurable from experimental data that has been used

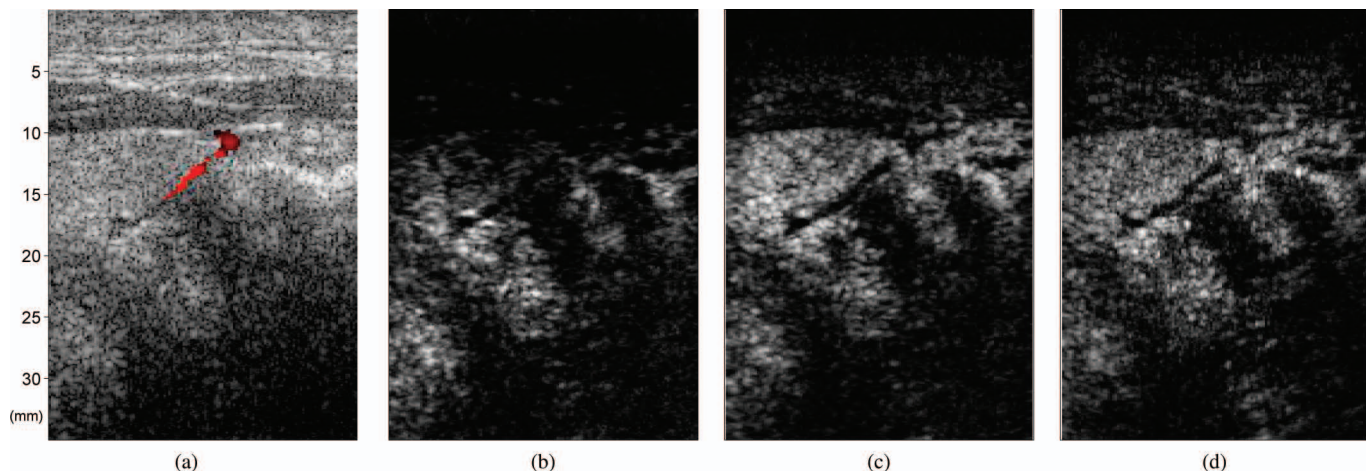


Fig. 8. *In vivo* human thyroid with transmit focus at 25 mm. (a) Color flow Doppler showing flow in carotid artery and small vasculature in thyroid over B-mode image. Background sample taken from 3-mm-square region to the left of the region of interest. (b) Dynamic receive, (c) focused transmit synthetic aperture, and (d) diverging transmit synthetic aperture short-lag spatial coherence (SLSC) images ($M = 10$).

to describe the electronic SNR of acquired signals [19]. However, a change in the derivation of this relationship is necessary to describe the expected SNR using channels across an array rather than on a beamformed A-line. The correlation is performed between the signals S_0 and S_n on channels of an array n elements apart with additive independent noise N_0 and N_n .

$$\rho = \frac{\int (S_0 + N_0)(S_n + N_n)}{\sqrt{\int (S_0 + N_0)^2} \sqrt{\int (S_n + N_n)^2}} \quad (14)$$

This equation can be simplified by assuming that the noise and signal are uncorrelated.

$$\rho = \frac{\int S_0 S_n}{\sqrt{\int (S_0^2 + N_0^2)} \sqrt{\int (S_n^2 + N_n^2)}} \quad (15)$$

The correlation of signals on the two channels is described by the linear coherence curve in fully-developed speckle with value 1 at zero lags and $1 - n/N$ at n lags on an N -element array. The signal power, P_S , on these two elements is assumed to be the same and the noise power is given by P_N .

$$\rho = \frac{P_S \left(1 - \frac{n}{N}\right)}{P_S + P_N} \quad (16)$$

$$= \frac{1 - \frac{n}{N}}{1 + \frac{P_N}{P_S}} \quad (17)$$

This can be rearranged to give a signal-to-noise ratio for a measured correlation coefficient at a given lag to find an experimental electronic SNR from a single set of channel data.

$$\text{SNR} = 10 \log_{10} \frac{P_S}{P_N} = 10 \log_{10} \frac{\rho}{1 - \rho - \frac{n}{N}} \quad (18)$$

APPENDIX B SYNTHETIC APERTURE COHERENCE

In contrast to the linear coherence curve obtained for either the focused transmit or the single-element synthetic aperture, experimental results for the multi-element diverging wave synthetic aperture show a distinctive curved shape. This type of curve is typically the result of apodization of the transmit aperture. We can use the linearity of the focusing process to calculate an effective aperture from the subapertures to find the magnitude and phase of the focused aperture. Relying on the autocorrelation relationship derived earlier, we can also predict the coherence curve from this aperture.

An aperture of a total of N elements is divided into overlapping subapertures of M elements with single-ele-

ment spacing and an element pitch of w . Focusing is performed in two stages—subaperture focusing to create a diverging wave and bulk focusing of the subapertures to form a focused beam. For each case, the distance between the center of the relevant aperture and the focal point is calculated.

Subaperture focusing uses the difference between the virtual source point at axial distance z_f behind the array and the element within the subaperture located at aw , where a is an indexing term from the center of the subaperture.

$$r_a = \sqrt{z_f^2 + (aw)^2} \quad (19)$$

Bulk focusing uses the difference between the focal point in the field, z_p , and the virtual source point behind the array located at $(bw, -z_f)$ where b is an indexing term from the center of the array. The distance is taken with reference to the path length from the center of the array. To accommodate the Fresnel approximation, the distance is approximated using the Taylor expansion.

$$r_b = \sqrt{(z_f + z_p)^2 + (bw)^2} - (z_f + z_p) \quad (20)$$

$$r_b \approx \frac{(bw)^2}{2(z_f + z_p)} \quad (21)$$

The phase across the array is also multiplied by the phase resulting from propagation from each physical element n element widths from the center of the array to the focal point z_p , represented by distance r_n . This term comes directly from the Fresnel approximation.

$$r_n \approx \frac{(nw)^2}{2(z_f + z_p)} \quad (22)$$

Each element is represented by a delta function with a particular magnitude and phase. The combination of the phase terms from (19), (21), and (22), applied with appropriate signs resulting from the difference in diverging and converging wave propagation, gives a complex description

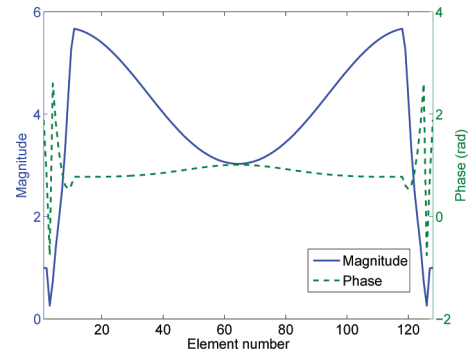


Fig. 9. Effective aperture magnitude and phase for multi-element diverging wave synthetic aperture. A typical single-element synthetic aperture produces a uniform magnitude and phase. 

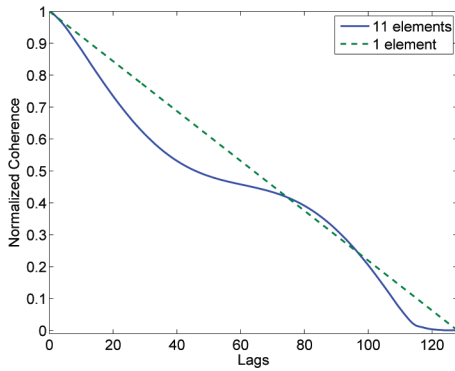


Fig. 10. Sample coherence curves calculated from aperture space using convolution. The difference in the short-lag region is minimal and would have only a small impact on short-lag spatial coherence (SLSC) imaging. 

of the resulting array. In a single-element synthetic aperture, r_a is zero and there is no overlap, so the weighting of each element is the same. In that case, the virtual source location is the element location, so r_b and r_n cancel and leave a uniform phase across the array. For a multi-element subaperture, these phases do not completely cancel and leave a residual phase corresponding to each physical element. The resulting effective array $U[n]$ therefore has nonuniform magnitude and phase.

$$U[n] = \sum_{b=-(N-M)/2}^{(N-M)/2} \sum_{a=-(M-1)/2}^{(M-1)/2} \delta[n - (a + b)] e^{jk(r_b - r_n - r_a)} \quad (23)$$

The magnitudes and phases across the array vary because of the two phase terms in the previous expression, making them sensitive to changes in element count, array pitch, frequency, and virtual source point. Fig. 9 shows a sample case for a 128-element, 7.5-MHz array with a $\lambda/2$ pitch using subapertures of 11 elements with an f-number of 0.75, focused behind the array. Notice the amplitude apodization compared with the uniform amplitude case, emphasizing high-frequency spatial content.

The difference between the effective aperture and a conventional uniform aperture affects the resulting coherence curve, shown in Fig. 10. Integration in the SLSC image formation process minimizes the effect of the difference in the curves, but this effect should be considered in any application relying on signal coherence. The effective apodization would also affect B-mode imaging, although this is not explored here. It is possible to reduce this effect by applying an appropriate apodization to each subaperture transmit depending on hardware capabilities.

ACKNOWLEDGMENTS

The authors thank D. Hyun for his SLSC processing code and N. Danieleley for his technical support.

REFERENCES

- [1] R. Mallart and M. Fink “The van Cittert-Zernike theorem in pulse echo measurements,” *J. Acoust. Soc. Am.*, vol. 90, pp. 2718–2727, Nov. 1991.
- [2] D.-L. Liu and R. C. Waag, “About the application of the van Cittert-Zernike theorem in ultrasonic imaging,” *IEEE Trans. Ultrason. Ferroelectr. Freq. Control*, vol. 42, no. 4, pp. 590–601, Jul. 1995.
- [3] J. Camacho, M. Parrilla, and C. Fritsch, “Phase coherence imaging,” *IEEE Trans. Ultrason. Ferroelectr. Freq. Control*, vol. 56, no. 5, pp. 958–974, May 2009.
- [4] P.-C. Li and M.-L. Li, “Adaptive imaging using the generalized coherence factor,” *IEEE Trans. Ultrason. Ferroelectr. Freq. Control*, vol. 50, no. 2, pp. 128–141, 2003.
- [5] M. A. Lediju, G. E. Trahey, B. C. Byram, and J. J. Dahl, “Short-lag spatial coherence of backscattered echoes: Imaging characteristics,” *IEEE Trans. Ultrason. Ferroelectr. Freq. Control*, vol. 58, no. 7, pp. 1377–1388, Jul. 2011.
- [6] J. J. Dahl, D. Hyun, M. Lediju, and G. E. Trahey, “Lesion detectability in diagnostic ultrasound with short-lag spatial coherence imaging,” *Ultrason. Imaging*, vol. 133, no. 2, pp. 119–133, 2011.
- [7] J. Dahl, M. Jakovljevic, G. F. Pinton, and G. E. Trahey, “Harmonic spatial coherence imaging: An ultrasonic imaging method based on backscatter coherence,” *IEEE Trans. Ultrason. Ferroelectr. Freq. Control*, vol. 59, no. 4, pp. 648–659, Apr. 2012.
- [8] C. H. Frazier and W. D. O’Brien Jr., “Synthetic aperture techniques with a virtual source element,” *IEEE Trans. Ultrason. Ferroelectr. Freq. Control*, vol. 45, no. 1, pp. 196–207, 1998.
- [9] M.-H. Bae and M.-K. Jeong, “A study of synthetic-aperture imaging with virtual source elements in B-mode ultrasound imaging systems,” *IEEE Trans. Ultrason. Ferroelectr. Freq. Control*, vol. 47, no. 6, pp. 1510–1519, 2000.
- [10] W. H. Kim, J. M. Chang, C. Kim, J. Park, Y. Yoo, W. K. Moon, N. Cho, and B. I. Choi, “Synthetic aperture imaging in breast ultrasound: A preliminary clinical study,” *Acad. Radiol.*, vol. 19, no. 8, pp. 923–929, 2012.
- [11] J. Kortbek, J. A. Jensen, and K. Gammelmark, “Synthetic aperture sequential beamforming,” in *IEEE Ultrasonics Symp.*, 2008, vol. 1, pp. 966–969.
- [12] P. D. Corl, P. M. Grant, and G. S. Kino, “A digital synthetic focus acoustic imaging system for NDE,” in *IEEE Int. Ultrasonics Symp.*, 1978, pp. 263–268.
- [13] M. Karaman, P.-C. Li, and M. O’Donnell, “Synthetic aperture imaging for small scale systems,” *IEEE Trans. Ultrason. Ferroelectr. Freq. Control*, vol. 42, no. 3, pp. 429–442, 1995.
- [14] J. W. Goodman, *Introduction to Fourier Optics* (McGraw-Hill Physical and Quantum Electronics Series). Greenwood Village, CO: Roberts and Co., 2005.
- [15] W. F. Walker and G. E. Trahey, “Speckle coherence and implications for adaptive imaging,” *J. Acoust. Soc. Am.*, vol. 101, no. 4, pp. 1847–1858, Apr. 1997.
- [16] R. S. C. Cobbold, *Foundations of Biomedical Ultrasound* (Biomedical Engineering Series). New York, NY: Oxford University Press, 2007.
- [17] C. Kasai, K. Namekawa, A. Koyano, and R. Omoto, “Real-time two-dimensional blood flow imaging using an autocorrelation technique,” *IEEE Trans. Sonics Ultrason.*, vol. 32, no. 3, pp. 458–464, May 1985.
- [18] L. F. Nock and G. E. Trahey, “Synthetic receive aperture imaging with phase correction for motion and for tissue inhomogeneities—Part I: Basic principles,” *IEEE Trans. Ultrason. Ferroelectr. Freq. Control*, vol. 39, pp. 489–495, Jul. 1992.
- [19] B. H. Friemel, L. N. Bohs, K. R. Nightingale, and G. E. Trahey, “Speckle decorrelation due to two-dimensional flow gradients,” *IEEE Trans. Ultrason. Ferroelectr. Freq. Control*, vol. 45, no. 2, pp. 317–327, Jan. 1998.



Nick Bottenus received the B.S.E. degree in biomedical engineering and electrical and computer engineering from Duke University, Durham, NC, in 2011. He is currently a Ph.D. student in biomedical engineering at Duke University and is a member of the Society of Duke Fellows. His current research interests include coherence-based imaging and beamforming methods.



Jeremy J. Dahl (M'11) was born in Ontonagon, MI, in 1976. He received the B.S. degree in electrical engineering from the University of Cincinnati, Cincinnati, OH in 1999. He received the Ph.D. degree in biomedical engineering from Duke University in 2004. He is currently an Assistant Research Professor with the Department of Biomedical Engineering at Duke University. His research interests include adaptive beamforming, noise in ultrasonic imaging, and radiation force imaging methods.



Brett C. Byram received the B.S. degree in biomedical engineering and math from Vanderbilt University, Nashville, TN, in 2004. He received the Ph.D. degree in biomedical engineering in 2011 from Duke University, Durham, NC. Between 2006 and 2007, he spent 10 months working with Jørgen Jensen in the Center for Fast Ultrasound in Lyngby, Denmark. He is currently an assistant research professor in the biomedical engineering department at Duke University. His ultrasound research interests include beamforming, motion estimation, and other related signal processing tasks.



Gregg E. Trahey (S'83–M'85) received the B.G.S. and M.S. degrees from the University of Michigan, Ann Arbor, MI, in 1975 and 1979, respectively. He received the Ph.D. degree in biomedical engineering in 1985 from Duke University. He served in the Peace Corps from 1975 to 1978 and was a project engineer at the Emergency Care Research Institute in Plymouth Meeting, PA, from 1980 to 1982. He currently is a Professor with the Department of Biomedical Engineering at Duke University and holds a secondary appointment with the Department of Radiology at the Duke University Medical Center. He is conducting research in adaptive phase correction, radiation force imaging methods, and 2-D flow imaging in medical ultrasound.